Variability of the Faraday rotation measure in the parsec-scale jet of AGN 1633+382

K. C. Lai [ID], J. C. Algaba [ID]★ and Z. Z. Abidin [ID]

Department of Physics, Universiti Malaya, 50603 Kuala Lumpur, Malaysia

ABSTRACT

We study the Faraday rotation measure (RM) variability of flat-spectrum radio quasar 1633+382 on five epochs spanning from 2004 to 2008. We used 4–43 GHz very long baseline interferometry polarization data from Very Long Baseline Array. Core RM across 4–15 GHz scales with a power index $a \sim 2$, for a in RM $\propto \nu^a$. We detected sign changes across epochs, both in the core and in the jet region. RM time variability in the core and jet region is not correlated, hence limiting the size of a possible Faraday screen. We relate the core RM variability to a new component emerging from the core region. For the jet region, we consider the jet–medium interaction to be a less likely cause of the RM variability because of the uniform spectral index distribution. The observed RM value variation requires a huge fluctuation in electron density or magnetic field; hence, a foreground Faraday screen is less favoured. We further discuss other possibilities of the RM variability based on jet kinematics.

Key words: galaxies: active – galaxies: jets – quasars: individual: AGN 1633+382.

1 INTRODUCTION

Polarized emission from active galactic nuclei (AGNs) jets provides crucial information about the jet environment. When linearly polarized emission passes through a thermal magnetized plasma, the polarization angle is rotated. This effect is known as Faraday rotation. The amount of rotation is proportional to the square of wavelength (λ^2), so the observed electric vector position angle (EVPA) is given by

$$\chi_{\mathrm{obs}} = \chi_{\mathrm{int}} + \mathrm{RM} \times \lambda^2, \quad (1)$$

where χ_{obs} and χ_{int} are the observed and intrinsic EVPA, and RM is the Faraday rotation measure. In thermal plasma, the RM can be described by

$$\mathrm{RM} = 812 \int n_{\mathrm{e}} \boldsymbol{B}_{\parallel} \cdot \mathrm{d}l \quad \left(\mathrm{rad\,m^{-2}}\right), \quad (2)$$

where n_{e} is the electron density in $\mathrm{cm^{-3}}$, $\boldsymbol{B}_{\parallel}$ is the magnetic field component along the line of sight, in milligauss (mG), and $\mathrm{d}l$ is the path-length in parsec (pc). The analysis of Faraday rotation is important to determine the intrinsic polarization angle and the magnetic field structure of the emitting region.

Time variability in the Faraday RM was observed extensively by different authors. Asada et al. (2008a) found a time variable RM in 3C 273 over a period of 7 yr, where the RM gradient persisted but its magnitude increased. They concluded that the variation was caused by the helical magnetic field in the jet sheath. By constraining the twist angle of the helical field (angle measured from toroidal to longitudinal component), Asada et al. (2008b) found that the

magnetic field that contributes to the Faraday rotation is not cospatial with the emitting region. However, the uncorrelated changes in RM and RM-corrected EVPA observed in 3C 120 by Gómez et al. (2011) implied that the emitting jet and the Faraday rotating material were not physically connected in that source. The double sign reversal observed favours the RM origin at the foreground cloud instead of the magnetic tower model. Gómez et al. (2008) also proposed for the source that the localized RM and the analysis of other polarization properties indicate the jet/cloud interaction as the origin of Faraday rotation. In Mrk 421, Lico et al. (2014) connected the increase in flux density from emerging components with the increase in RM, hence supporting the magnetic tower model. This is further supported by two RM sign reversals. The magnetic tower model describes an inner magnetic field with the same helicity as the accretion disc, and an outer magnetic field of opposite helicity. The change in relative contribution from the inner and outer helical magnetic field can be related to RM sign changes. O'Sullivan & Gabuzda (2009) suggested bends or acceleration in jets can also lead to RM sign changes. Lisakov et al. (2021) then employed an oversized jet sheath model to explain the RM variability in 3C 273, which should evolve slowly and not be affected much by the change in jet direction. The radial profile of the RM magnitude supports its origin in hot winds, rather than the jet sheath (Park et al. 2019). The authors further explained that the dominance of negative RM without a significant gradient is caused by jet and wind axis misalignment.

The source 1633+382 is a flat-spectrum radio quasar, with a redshift of $z = 1.813$ (Hewett & Wild 2010), with black hole mass estimated in the range $\log M / \mathrm{M_\odot} = 7.5$–9.5 (Foschini 2011; Fan et al. 2013; Zamaninasab et al. 2014; Chen et al. 2015). The parsec-scale jet is aligned at $\sim 2.5°$ to our line of sight (Hovatta et al. 2009; Liu et al. 2010), with superluminal motion of the jet up to $393 \pm 26\,\mu\mathrm{as\,yr^{-1}}$ ($30.8 \pm 2.0\,c$) detected at 15 GHz (Lister et al.

★ E-mail: algaba@um.edu.my

Table 1. Observation epoch. [1] Observation date. [2] Project code. [3] Observation frequency. [4] Convolving beam, in minor axis FWHM, major axis FWHM, and degree eastward from north. [5] EVPA calibrator. [6] Reference antenna, same for all frequencies. [7] EVPA correction, in order of observing frequency.

Date [1]	Project [2]	Frequency (GHz)[a] [3]	Beam (mas, mas, °) [4]	EVPA cal. [5]	Ref. ant. [6]	EVPA corr. (°) [7]
2004 Nov 1	BG152	15, 22, 43	0.50, 0.85, −12.1	2134+004	LA	$58 \pm 5, -51 \pm 6, -63 \pm 5$
2005 Feb 2	BK107f	22, 43	0.60, 0.98, 19.77	1749+096	LA	$15 \pm 4, -42 \pm 1$
2005 Feb 5	BL123B	15		[b]	b	[b]
2006 Sept 6	BL137i	8.1, 8.4, 12, 15	0.96, 1.35, 0.69	1156+295	LA	$-3 \pm 3, 2 \pm 3, 126 \pm 3, 106 \pm 5$
2007 Sept 26	BG173b	4, 5, 7, 8, 12, 15	2.04, 3.77, −26.53	0851+202	FD	$-111 \pm 2, 63 \pm 1, -106 \pm 4$
						$-29 \pm 1, -5 \pm 4, -32 \pm 2$
2008 Nov 2	BA089	12, 15, 22, 24	0.75, 0.75, 0.00	D-term	LA	$55 \pm 6, -49 \pm 4, 69 \pm 8, -47 \pm 16$

[a]For more accurate frequency value refer Table 2.

[b]The calibrated archive data were obtained from the MOJAVE website.

2021). Intraday variability in radio spectrum was observed by Aller, Aller & Hughes (1992), and Volvach et al. (2009) found strong variability in radio, optical, and γ-ray frequencies.

The RM in this source was observed separately in 2006 (Hovatta et al. 2012), 2007 (Coughlan & Gabuzda 2013), and 2008 (Algaba 2013). For the three studies, the observed RM was different from each other, but no variability analysis was conducted throughout the literature. Hence, in this study, observations from 2004 and 2005 were added, and RM variability was analysed together with other polarization properties.

2 METHODOLOGY

Multifrequency Very Long Baseline Array (VLBA) archival data were used, covering five epochs as shown in Table 1. All data sets consist of multifrequency single-epoch observations, except for the year 2005, when observations from two separate close-epoch projects were combined. The data were calibrated using standard AIPS calibration techniques for polarization. Raw VLBA archive data were downloaded, then amplitude calibration, opacity correction, parallactic angle correction, fringe fitting, cross-hand delay correction, and bandpass calibration were done. Imaging was carried out in DIFMAP with uniform weighting throughout the process. Simultaneous solution for instrumental polarizations (D-terms) and the source polarization of D-terms calibrator was determined using the AIPS task LPCAL. Then, the EVPAs for each epoch were calibrated using near-simultaneous observation from the Very Large Array (VLA) POLCAL project data. When there is no simultaneous observation or frequencies, for each VLA frequency, we first interpolated the VLA EVPA in time. Then we plotted the obtained EVPAs against λ^2 of VLA, and from there we estimated the integrated EVPAs of VLBA observing frequencies and their error.

The exception is the project BA089, for which there was no EVPA calibrator to compare with the VLA data. Hence, for this epoch the EVPA was calibrated by comparing D-terms phases between two observations (Gómez et al. 1992). Here we used project BO033 (2008 December 7). To ensure consistency, we used the D-terms calibrator 0420−014 in both projects. We then obtained the D-terms phases of all antennae, for both projects. The D-terms phase offset between project BA089 and BO033 was determined, and then averaged across antennae to recover the EVPA correction through the standard polarization interferometric equation (Leppanen, Zensus & Diamond 1995). Since there was no direct comparison on the EVPA calibrator between VLBA and VLA observation, the error introduced in the final EVPA correction is directly affected by the spread of D-terms among antennae. This caused larger uncertainties in the

final EVPA compared to other epochs. Calibration information is presented in Table 1.

After the calibration, CLEAN images of Stokes I, Q, and U were produced with two methods: the standard polarization CLEAN in DIFMAP and the complex CLEAN method in MIRIAD. The complex CLEAN method described by Pratley & Johnston-Hollitt (2016) preserves the rotational invariance of polarization CLEANING, while reducing spurious components. We then compared the derived polarization properties. More detailed information on the comparison is discussed in the appendix. We concluded that the standard polarization CLEANING is reliable within uncertainty, and proceeded with the standard method to maintain continuity with different studies in the literature. The errors in the CLEAN maps of Stokes I, Q, and U were then determined using the rms of residual maps. However, note that the actual error in Stokes Q and U maps needs to be further analysed to include the CLEANING error and the D-terms error; see below.

Stokes I, Q, and U CLEAN maps were convolved with the same beam size, respective to the observation, as in Table 1. For maps of the year 2004, 2005, and 2006, the beam of the lowest frequency was chosen as the convolving beam. For years 2007 (Coughlan & Gabuzda 2013) and 2008 (Algaba 2013), we used the same beam as their respective paper. This is to facilitate the comparison of results.

The information about the absolute phase is lost during self-calibration while imaging, introducing an offset of the core from the map centre. The position of the observed radio core will also shift with frequency, this is the well-known core shift effect (Lobanov 1998). The image shift, which is the vector sum of offset and core shift, is required to properly align maps of all frequencies. Stokes I maps were used to obtain the image shift, and then applied to Stokes I, Q, and U maps. We used the program VIMAP developed by Kim (2014), based on the cross-correlation of the optically thin region of jet (Walker et al. 2000; Croke & Gabuzda 2008), to obtain the image shift.

We then used the aligned Stokes Q and U maps to construct the polarized intensity map $\left(p = \sqrt{Q^2 + U^2} \right)$, and the EVPA map ($\chi = (1/2) \arctan(U/Q)$). Rician debiasing was performed on all polarization intensity maps as in Wardle & Kronberg (1974). Their respective noise maps were also produced. To estimate the error in Stokes Q and U maps (σ_Q and σ_U), we further added the D-terms error and the CLEAN error as below (Hovatta et al. 2012):

$$\sigma = \sqrt{\sigma_{\mathrm{rms}}^2 + \sigma_{\mathrm{D\text{-}terms}}^2 + (1.5 \times \sigma_{\mathrm{rms}})^2}, \qquad (3)$$

$$\sigma_{\mathrm{D\text{-}terms}} = \frac{0.01}{\sqrt{N_{\mathrm{ant}} \times N_{\mathrm{IF}} \times N_{\mathrm{scan}}}} \sqrt{I^2 + (0.3 \times I_{\mathrm{peak}})^2}, \qquad (4)$$

where σ_{rms} is the error in the final residual map, the factor 0.01 is the rough estimate from the scatter of fitted D-terms, N_{ant} is the number

of antennae, $N_{\rm IF}$ is the number of intermediate frequencies (IFs), $N_{\rm scan}$ is the number of scans for 1633+382, I is the total intensity map, and $I_{\rm peak}$ is the peak total intensity of the map. Then σ_Q and σ_U were propagated into other polarization properties. Note that the error from the EVPA calibration was included in the final EVPA error. To calculate the fractional polarization error, we propagated the error from σ_Q, σ_U, and the Stokes I residual map rms $\sigma_{\rm rms}$.

To calculate the RM, we resolved the $n\pi$ ambiguities of EVPA across frequencies. Our data show that the largest EVPA difference between the highest and lowest frequency across all epochs was only $\sim 45°$. Introducing more than one π rotation to the EVPA can artificially smooth out the RM fitting residual, while producing extremely high RM in the core region. Indeed, by introducing $n\pi$ rotation we can produce a linear λ^2 fit, but we found that the |RM| obtained this way is of the order 10^4 rad m^{-2} or higher. RM of this order of magnitude will easily rotate the EVPA of close frequency pairs significantly. Referring to project BL137i and BG173b, such significant EVPA differences were not observed between close frequency pairs, for example, 8.1 and 8.4 GHz, 4.6 and 5.1 GHz, and 7.9 and 8.9 GHz; in fact, the separation is merely a few degrees. Similarly to the other epochs, the $n\pi$ rotated EVPA gives an artificially high RM. Therefore, we assumed that the EVPA difference between the frequencies is only within $\pm 90°$.

We then proceeded to produce the RM maps using the same-beam registered polarization maps. RM was determined by the slope of the linear fit between EVPA and λ^2. In the core region, some epochs show deviation from the linear λ^2 law, hence in these cases we either used: (a) more than one linear fit, or (b) the scaling relation of RM $\propto \nu^a$, where a is the power index (see Section 3.3). In the jet region, the EVPA obeyed the linear λ^2 law, hence, a single linear fit was sufficient.

3 RESULTS

3.1 Polarization properties

We obtained total intensity, polarization intensity, fractional polarization, and Faraday corrected EVPA maps for five epochs (see Table 2). In general, we observed significant polarization in two regions of the source: in the core region and in the standing knot of the jet located at around 3.5 mas from the core. In both cases, the region with polarized emission extends only one or two beamwidths. The fractional polarization and Faraday-corrected EVPA maps are shown in Fig. 1. Additional EVPA, polarization, and fractional polarization maps are shown in Figs C1 and D1, respectively. We observe that both the core and jet fractional polarization show a gradient. Because of the unresolved nature of the core, the gradient at the core does not allow for further interpretation. The gradient in jet region will be discussed in Section 4.5. The Faraday-corrected EVPA was oblique to the jet direction, both in the core and jet regions. In the jet region, the Faraday-corrected EVPA was roughly perpendicular to the fractional polarization gradient, for years 2006, 2007, and 2008.

3.2 General RM maps

RM maps for all epochs are shown in Fig. 2. At the core region, we observe an increase in |RM| with frequency in three epochs. This deviation from the linear λ^2 law may indicate opacity effects. The exceptions are 2006 and 2008, where in 2006 the EVPAs obeyed the linear λ^2 law, and in 2008 the EVPA calibration error was too large. Because of (a) sparse frequency sampling or (b) the overall frequency span is too small, we were not able to definitely rule out internal Faraday rotation. We assumed an external Faraday screen

because of the slow variability in 43–22 GHz RM. In the jet region, the linear λ^2 law was observed in 2006, 2007, and 2008. We also observed the inverse depolarization in the core region, except in 2004, where depolarization increased toward low frequency. Here we specify further comments on the years 2006, 2007, and 2008.

3.3 2006 September

The core EVPA scales linearly with λ^2. The core region shows higher |RM| than the jet region. The core RM tends to have a higher magnitude northward, but because of the unresolved nature of the core region, we do not consider the presence of a gradient. See more details in Section 4.3.

We further investigated the possibility of deviation from the linear λ^2 law. From RM $\propto \nu^a$ (Jorstad et al. 2007), we used |RM| $= A \times \nu^a + d$ for generality. Then we derived the scaling relation for $\chi_{\rm obs} = A\lambda^{-a+2} + \lambda^2 d + c$. We note that this formula is only meaningful for the determination of the value a, and the other parameters imply the physical condition at different frequencies. Two additional constraints are applied to the above relation: (i) the observed RM is of negative sign; and (ii) the magnitude |RM| decreases with longer wavelength. These constraints indicate that $A < 0$, $d < 0$, and $a \geqslant 0$. We then used the Markov chain Monte Carlo method to find the posterior distribution of parameters A, a, d, and c. The posterior distribution of a peaks strongly at zero; hence, a single linear RM fit can explain the observed EVPA.

3.4 2007 September

In this epoch, the core RM sign also changes from positive to negative, going towards lower frequency, with a decrease in |RM|. As shown in Fig. 2(d), the core EVPA does not scale linearly with λ^2. The increase in RM with shorter wavelength is expected from the scaling relation RM $\propto \nu^a$. Using the two core RM fitted in Fig. 2(d), we obtained the power index $a \sim 1.48 \pm 1.40$.

In the jet region, RM scales linearly with λ^2, which is consistent with the optically thin regime. Spatially, the RM obtained with 4.6 and 5.1 GHz exhibited a sign change from negative to positive going from the core to the jet region.

3.5 2008 November

The core region shows a higher |RM| than the jet, while having a similar positive sign. The large uncertainty at 24 GHz, and the fact that only three frequencies are observed, does not permit the observation of EVPA scaling with λ^2. A slice was taken at the jet region, from south to north, as shown in Fig. 2(e). A RM gradient was observed in this region (see Fig. 3), which is consistent with Algaba (2013). The fractional polarization of 12 GHz shows signs of depolarization at the southern ~ 0.3 mas of the slice, and the peak fractional polarization coincides with zero |RM| value. The depolarization effect is weaker for 15 GHz and is not observed in higher frequencies. Reaching the centre of the knot, all frequencies show similar magnitude of fractional polarization, even with the increasing |RM|. Going northward, all frequencies show low fractional polarization, without significant difference in depolarization.

4 DISCUSSION

4.1 High-frequency core RM

The 2004 and 2005 observations are spaced by 3 months, the shortest within the five epochs. In this period, the core RM sign remains nega-
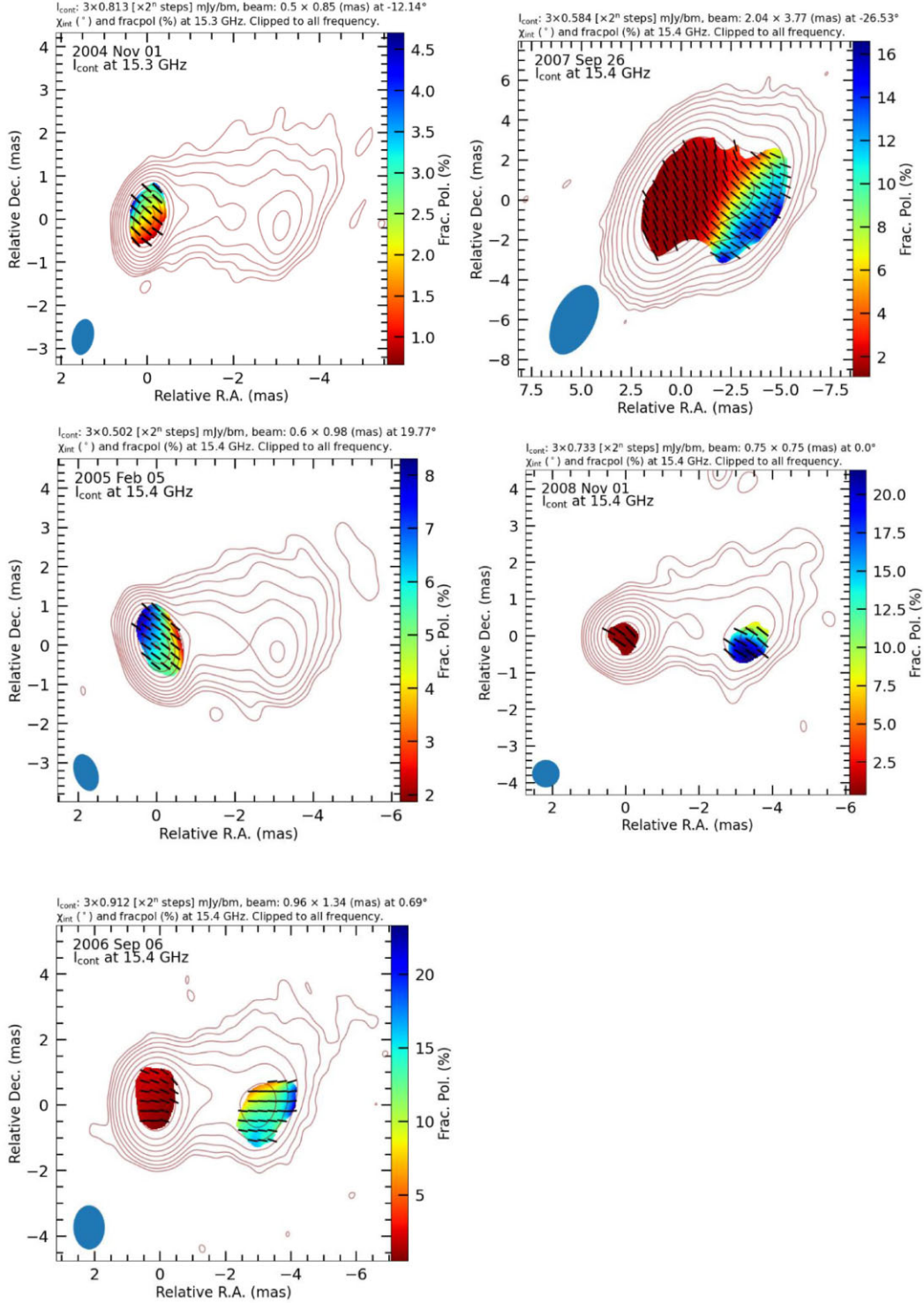
Figure 1. Maps of 1633+382 at various epochs discussed. The contour levels indicate the total intensity, starting at 3σ level, increases at steps of 2^n. The colour scale indicates the fractional polarization. Tick mark of uniform length represents χ_{int}. The solid ellipse on the bottom left corner indicates the beam size of the map. For fractional polarization and EVPA maps of other frequencies, see Appendix C.

tive. The apparent 43–22 GHz |RM| decrease in this period is within 1σ of the error, and RM for 22–15 GHz RM remains at zero. The χ_{int} obtained using 43–22 GHz are consistent within 1σ. Hence, the core RM sign, magnitude, and χ_{int} are consistent within 3 months, at least within the errors of our observation. Hence, the Faraday screen in the core region could be external to the jet (Hovatta et al. 2012).

Following the assumption of an external Faraday screen, Jorstad et al. (2007) derived $|RM| \propto d^{-a}$, where d is the distance from the central engine. Then the core distance from central engine depends on observing frequency ν, as derived by Lobanov (1998) as $d_{\text{core},\nu} \propto \nu^{1/k_r}$. The value of $k_r \sim 1$ in 1633+382 is obtained by Algaba, Gabuzda & Smith (2012), hence from the relations above
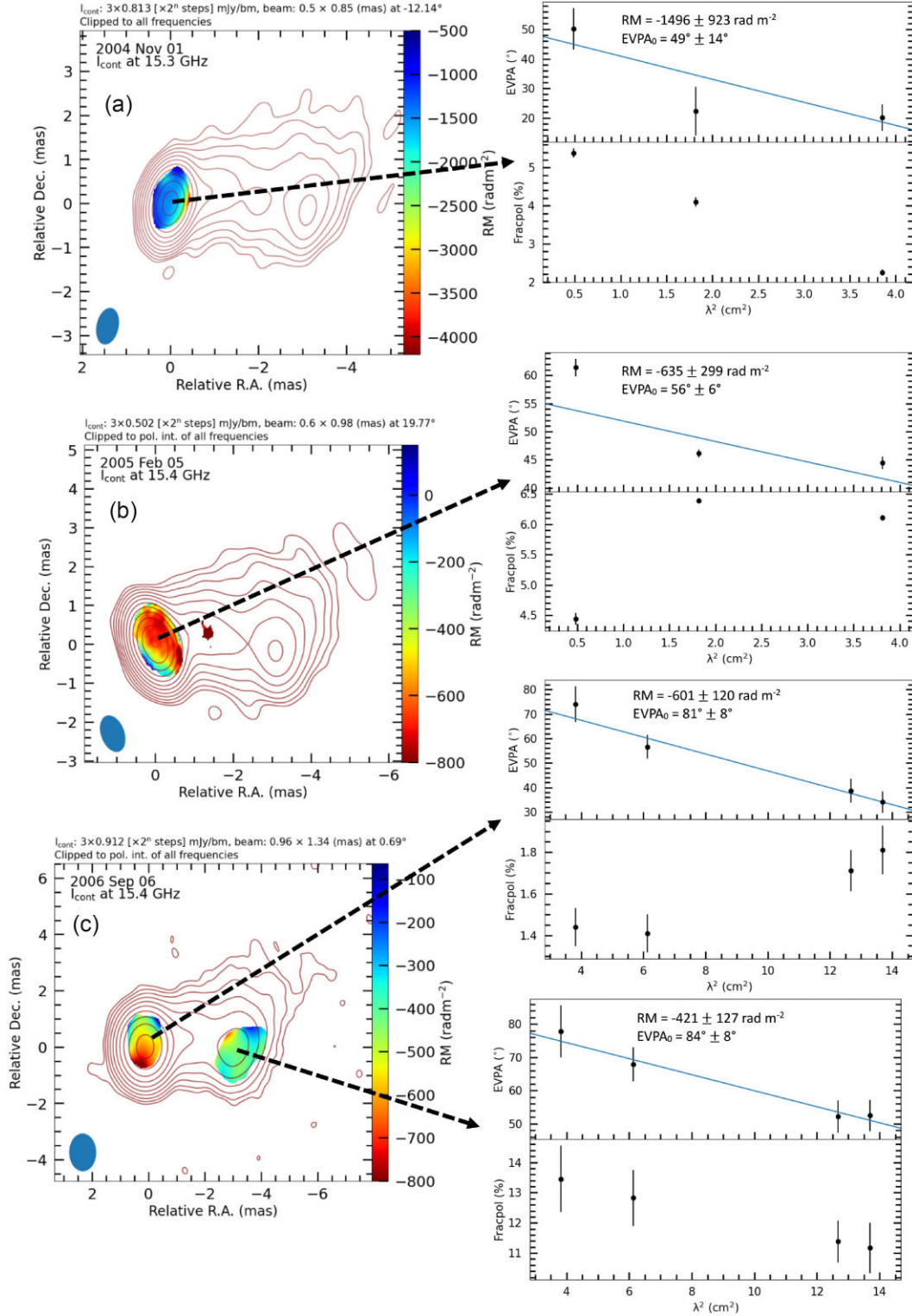
Figure 2. RM maps of all epochs. RM colour map overlaid on total intensity contour, arranged in timely order. The total intensity contours were plotted in levels $3\sigma \times 2^n$ steps, where the σ is the residual rms. The RM fit (shown as a straight line) and fractional polarization at the indicated position were shown in the plot. In panel (d), the colour scaling is different in the core and jet. In the core, the RM value fitted with the highest four frequencies was shown as a colour scale, and the RM obtained from the lowest two frequencies was only quoted at the right of the panel. In the jet region, all six frequencies were used. The black curved line indicates the separation of the core and jet region. In panel (e), the core region RM fit excluded 22 GHz, because we do not detect significant 22 GHz polarization in the core. The vertical black line at the jet region indicates the slice position.
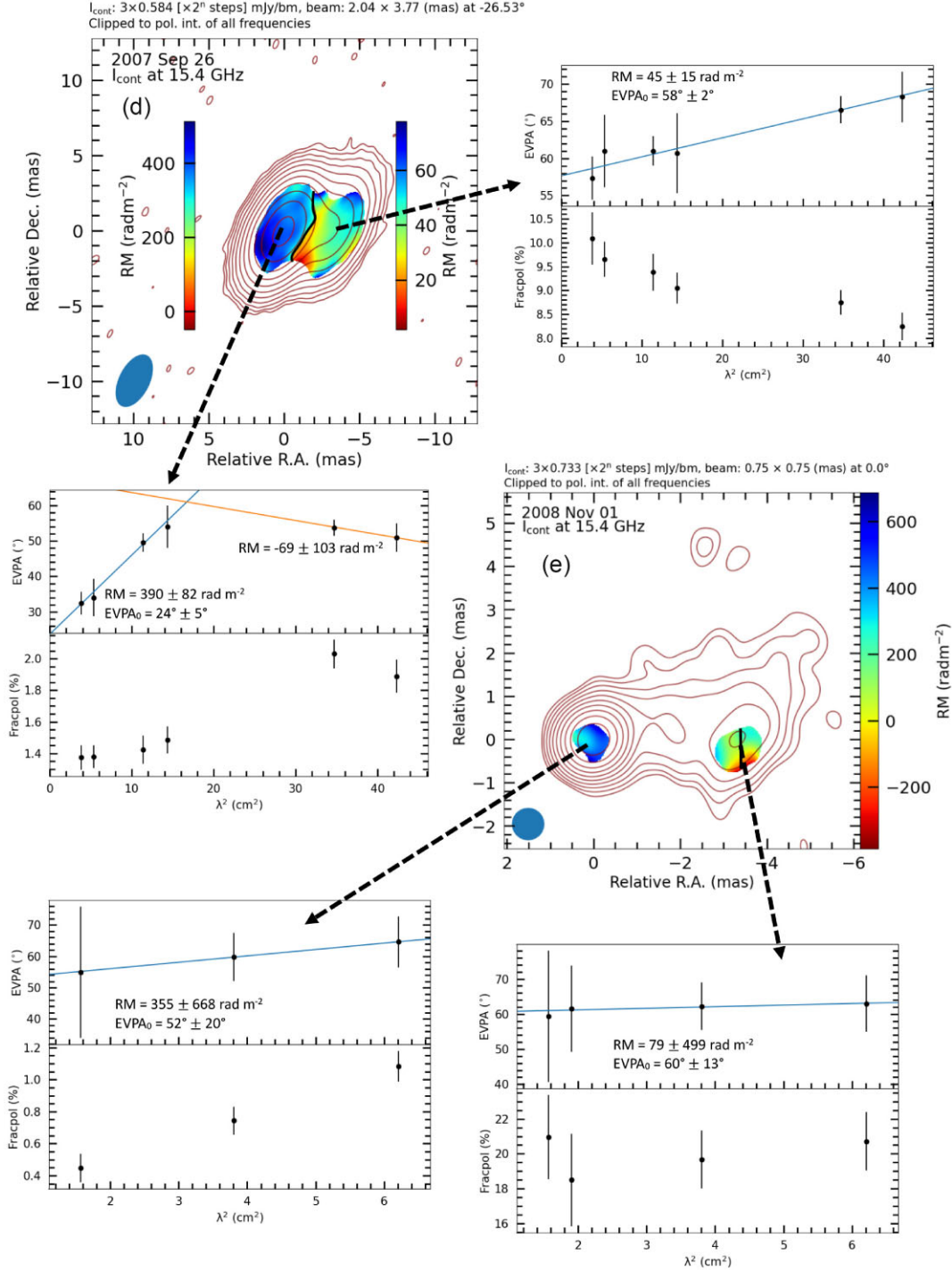
Figure 2. (*continued*).

we can write $|RM_{core,\nu}| \sim \nu^a$. Using this relation, we extrapolated the 2006 RM to 43–22 GHz to investigate the longer time-scale change. If we use the power index of year 2007 $a \sim 1.48$ (since in 2006 we could not obtain a power index) to extrapolate to 43–22 GHz, we obtained RM ~ -3000 rad m^{-2}. RM in 2006 remains negative, similar to 2004 and 2005.

Here, we provide an interpretation for the 43–22 GHz observation (15 GHz in Section 4.4). The 43–22 GHz |RM| shows remarkably slow variability in years 2004, 2005, and possibly also in 2006. However similar slow variability is not observed in the 43 GHz EVPA. We

obtained from Boston University Blazars[1] monitoring program 2007 to 2008 data, the 43 GHz polarized intensity and EVPA vary rapidly on a time-scale of 1–2 months. We can assume a single emitting component with an external Faraday screen, dominating the 43–22 GHz core flux. In this case, both the $\chi_{int,43-22\,GHz}$ and 43 GHz EVPA should show similar variability, but their variability should be uncorrelated with that of RM. Indeed, from 2004 and 2005 both $\chi_{int,43-22\,GHz}$

[1] https://www.bu.edu/blazars/VLBA_GLAST/1633.html

Table 2. Core and jet polarization properties, after full calibration and corrected for $n\pi$ rotation to within 0 and 1π. The values stated below are taken at the polarization intensity peak of 15 GHz. Refer to Fig. 2.

Project	Freq. (GHz)	χ_{core} (°)	χ_{jet} (°)	RM_{core} (rad m^{-2})	RM_{jet} (rad m^{-2})	$\chi_{int,core}$ (°)	$\chi_{int,jet}$ (°)	m_{core} (per cent)	m_{jet} (per cent)
BG152	15.285	20 ± 5	63 ± 8	-1496 ± 923	[a]	49 ± 14	[a]	2.25 ± 0.08	14.7 ± 2.2
	22.235	22 ± 8	[a]	$\sim 0^{22,15\,c}$				4.10 ± 0.12	[a]
	43.135	50 ± 7	[a]	$-3656 \pm 1400^{43,22\,c}$		$60 \pm 10^{43,22,\,c}$		5.39 ± 0.12	[a]
BL123B	15.365	44 ± 1	59 ± 3	-635 ± 299	[a]	56 ± 6	[a]	6.11 ± 0.05	15.3 ± 1.2
BK107f	22.233	46 ± 1	68 ± 4	$\sim 0^{22,15\,c}$				6.39 ± 0.04	14.0 ± 1.4
	43.217	61 ± 2	[a]	$-1824 \pm 184^{43,22\,c}$		$65 \pm 4^{43,22,c}$		4.44 ± 0.10	[a]
BL137i	8.108	34 ± 4	52 ± 5	-601 ± 120	-421 ± 127	81 ± 8	84 ± 8	1.81 ± 0.12	11.2 ± 0.8
	8.428	39 ± 5	52 ± 5					1.71 ± 0.10	11.4 ± 0.7
	12.123	57 ± 5	68 ± 5					1.41 ± 0.09	12.8 ± 0.9
	15.365	74 ± 7	78 ± 8					1.44 ± 0.09	13.5 ± 1.1
BG173b	4.612	51 ± 4	68 ± 5	390 ± 82	45 ± 15	24 ± 5	58 ± 2	1.89 ± 0.10	8.2 ± 0.3
	5.092	54 ± 2	66 ± 2					2.03 ± 0.09	8.7 ± 0.3
	7.916	54 ± 6	61 ± 5	$-69 \pm 103^{5,4\,c}$				1.48 ± 0.09	9.0 ± 0.3
	8.883	50 ± 3	61 ± 2					1.42 ± 0.09	9.4 ± 0.4
	12.939	34 ± 5	61 ± 5					1.38 ± 0.07	9.7 ± 0.4
	15.383	32 ± 3	57 ± 3					1.37 ± 0.08	10.1 ± 0.6
BA089	12.039	65 ± 8	63 ± 8	355 ± 668	79 ± 499	52 ± 20	60 ± 13	1.08 ± 0.10	20.7 ± 1.7
	15.383	60 ± 8	62 ± 7					0.74 ± 0.09	19.7 ± 1.7
	21.775	[a]	62 ± 12					[a]	18.5 ± 2.6
	23.998	55 ± 21	59 ± 19					0.45 ± 0.09	21.0 ± 2.4

[a] No polarization intensity more than 3σ observed.

[b] Error quoted according to Monte Carlo simulation.

[c] Value with superscripts are obtained through the fitting of frequencies (in GHz).

and 43 GHz EVPA show similar increment (within error of $\sim 10°$). This agrees with the external Faraday screen interpretation in the previous paragraph. This correlation is not guaranteed if there are multiple components, each dominating the polarized flux at different times. Unfortunately, we do not have 43 GHz data in 2006 to estimate $\chi_{int,43-22\,GHz}$. To confidently determine the variability of RM, χ_{int}, and EVPA, denser frequency and time sampling are imperative.

4.2 Equipartition condition

From the relation $RM \propto \nu^a$ (Lobanov [1998](#); Jorstad et al. [2007](#)), the unknown parameters are the power index m of magnetic field ($B \propto d^{-m}$), n of electron density ($n_e \propto d^{-n}$), and k_r related to the core shift effect. We assume here a conical jet and toroidal magnetic field (Jorstad et al. [2007](#)). The scaling of magnetic field and electron density here refers to the quantity in the jet sheath, and k_r refers to the jet emitting region. With these conditions the value of a is described by $a = (m + n - 1)/k_r$, hence $a = m + n - 1$. Then the value of a reflects the scaling relation of the jet sheath. If the jet sheath follows equipartition, then the reasonable estimates are $a = 2$, $m = 1$, and $n = 2$. In all five epochs, the only estimate of a is in year 2007, where $a = 1.48 \pm 1.40$, approximately $a \sim 2$, although with large uncertainty. This may indicate that the jet sheath is in equipartition condition.

4.3 Unresolved nature of core

We further investigated the possibility of resolving the RM structure in the core. Mahmud et al. ([2013](#)) simulated transverse RM gradient of a given width, and then convolved with a beam of size 20 times larger. Their result showed that the gradient remained present, but the magnitude diminished. Here, we intended to constrain the beam-to-core size ratio to identify any underlying structure. We used the total intensity (Stokes I) map as the baseline for resolving. From the Stokes I CLEAN image, we identified the region of significant emission (flux density larger than three times the residual rms) and the background noise region (flux density smaller than three times the residual rms). In the significant emission region, the brightest pixel of the central unresolved core was used as the origin. Then the pixels of radial distance larger than 1.5 times the beam pattern are replaced with a simulated background noise. This will remove the jet emission while including any structure at the core. Then we fitted a 2D Gaussian to the map, and obtained their full width at half-maximum (FWHM) for major and minor axes. We compared the FWHMs with the CLEAN beam FWHMs. This is based on a few arguments. (a) Assume that the true core structure in perfect resolution is a 2D Gaussian, then convolving a *resolved* Gaussian core structure with any smaller beam will only lead to a larger FWHM. This means that the beam and the component FWHM are added in quadrature. (b) Assume the true core structure is other than 2D Gaussian, then the convolved image will deviate from a 2D Gaussian and lead to a bad fit. Our result shows that the fitted FWHMs and beam FWHMs are consistent to within 1 per cent, showing that the true core structure is a δ-function, unresolved in this case. Hence, we found that the core size, even if present, is at most ~ 0.1 times the beam size.

Using the resolution criteria in Kovalev et al. ([2005](#)), with the longest baseline visibilities projected north–south (to resolve the transverse structure), we determined that the Stokes I and the polarized intensity core are unresolved. To further constrain the size, we applied the maximum theoretical overresolution power (Martí-Vidal, Pérez-Torres & Lobanov [2012](#)), and determined the 15 GHz Stokes I core can range between 0 and 0.015 mas (~ 2 per cent of 15 GHz beam FWHM). The core polarized intensity size has a much larger uncertainty range, 0–0.2 mas.

To support this claim, we further examined the distribution of CLEAN components in the observable region. We assumed that the CLEAN delta components comprise 'true' CLEAN components, and 'noise' components randomly distributed in flux density. The noise components will make up the majority of all components, hence we recursively fit the Gaussian distribution onto all CLEAN components,
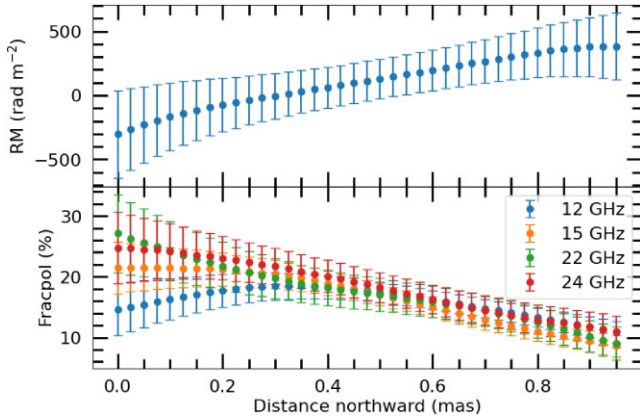
Figure 3. Slice taken from south to north of jet region, year 2008. Both RM and fractional polarization profiles show transverse gradient. The error bar in the RM plot excludes the EVPA calibration error, as it is correlated spatially, hence irrelevant in the determination of RM gradient (Mahmud et al. 2013). Note that the beam size spans 0.75 mas.
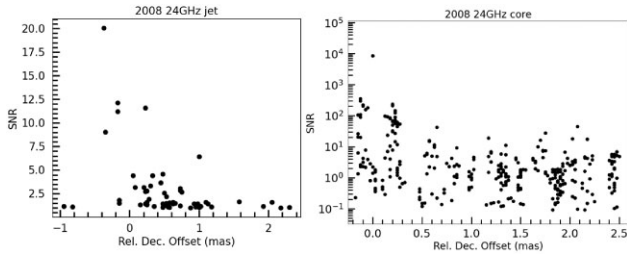

Figure 4. The declination offset of all CLEAN components larger than 2.5σ. The jet is pointing westward, hence we measure the declination offset to determine if the jet's transverse structure is resolved. Refer to the text for the meaning of SNR. Note that the plot for the jet is relative to 3.5 mas west of the image centre, and the plot for the core is in logarithmic scale.

and isolate out the true components. We then obtained the σ of the Gaussian fitting, then for all components, we plotted the ratio of flux density over σ against the declination offset from the map centre. The ratio is named 'SNR' in Fig. 4. As shown there, there is a single extremely strong component at more than 2000 SNR, and this single component will dominate all the flux density observed at the core. This is in contrast to the jet region, where multiple components of comparable magnitude exist across a distance larger than the beam FWHM. Furthermore, the 2D Gaussian fit on the isolated jet's knot produced a FWHM twice the beam FWHM. In all epochs, the core region is dominated by a single component, which means the core is likely unresolved. Hence, we avoided interpreting the polarization spatial structure, as it may arise from artefacts.

4.4 Core RM changes

In the core region, for both years 2004 and 2005 there is no EVPA rotation between 15 and 22 GHz, hence we do not expect there will be significant rotation at lower frequencies. However, in year 2006, rotation of more than $45°$ was observed, and this was accompanied by a 15 GHz fractional polarization decrease from 6.11 per cent (2005) to 1.44 per cent (2006). The 15 GHz low fractional polarization in year 2006 cannot be explained by RM gradient, since this substantial depolarization requires a RM gradient >2500 rad m^{-2} (Zavala & Taylor 2004). Hence, we attribute these changes to the ejection of a
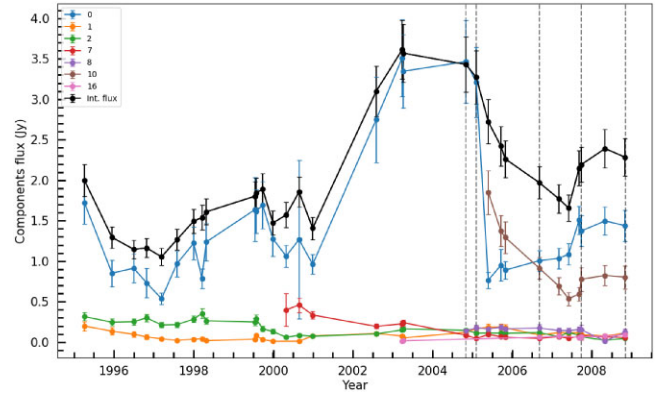
Figure 5. Components and integrated core flux density against time. The component number follows Lister et al. (2009). The vertical lines indicate the five epochs in this study.

new component C10 on 2005 May 26 as identified by Lister et al. (2009), observed at 15 GHz.

To further investigate this possibility, we obtained the MOJAVE 15 GHz MODELFIT components from Lister et al. (2009). For epochs not present in their data set, we used MODELFIT in DIFMAP to obtain the circular components. These epochs are 2005 May 26, 2006 September 6, 2007 September 26, and 2008 November 2. We identified three components that are located within the 1.0 mas core region. They are component numbers 0 (core), 10, and 7, which we will denote here as C0, C10, and C7. To compare the contribution of the components to the observed core flux density, we used the 15 GHz CLEAN delta components from MOJAVE. We calculated the core integrated flux density as the sum of all CLEAN delta components within the radius of 1.0 mas from the core (1.0 mas is the typical beam size of VLBA at 15 GHz). We then assumed the error to be 10 per cent of the total integrated flux density from the whole source, the typical self-calibration error. The error in MODELFIT components was calculated according to Lee et al. (2008) and Fomalont (1999). We plotted the time evolution of the core integrated flux density together with the MODELFIT components, as in Fig. 5. As shown in Fig. 5, the two components that dominate the core emission are C0 and C10.

Component C10 is only detected from the middle of 2005 onward, and it shows a slow but linear trajectory relative to the core position (C0). The component motion of C0, C7, and C10 are shown in Fig. 6. Uncertainty in position was estimated using 20 per cent of beam size (Homan et al. 2002; Lister et al. 2009). We fitted the components motion and found that the predicted position on our observation date in 2008 is only 0.27 ± 0.04 mas in radial distance relative to the core position (component C0). Hence, the ejected new component will not be resolved. As shown in Fig. 5, in the year 2005, the component C10 contributed the majority of the total flux density, but it decayed to a similar level on our observation date of the year 2006. Then, for 2007 and 2008, the core component again dominated the total flux density. Following the trend of C10, it is reasonable to suspect that the increase of core flux density starting from around 2001 is caused by the coming C10, where the core component maintains a rather stable flux density throughout the year. We extrapolated the position of C10 to the year 2001, and the radial distance from core C0 is estimated to be 0.05 ± 0.06 mas, hence, C10 should not be too far upstream of the jet at the time of flux density increase.

We speculate that the RM in both years 2004 and 2005 is dominated by C10, which at these dates had not moved out from the optically thick region yet. Unfortunately, we did not have sufficient
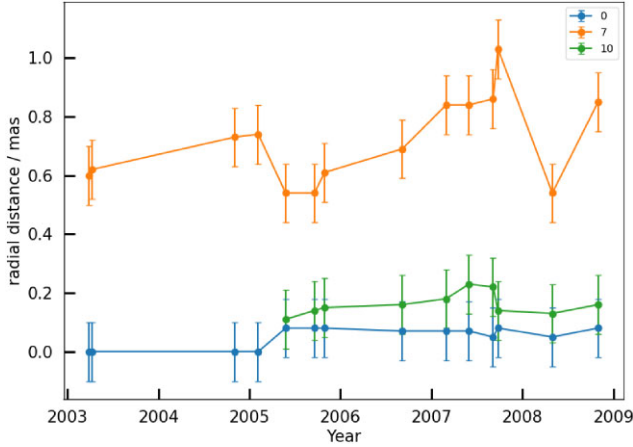
Figure 6. Motion of component C0, C7, and C10 over time. Plotted with data from Lister et al. (2009).

I_{cont}: 3×0.733 [×2^n steps] mJy/bm at 15.4 GHz, beam: 0.75×0.75 (mas) at $0.0°$

I_{cont}: 3×0.584 [×2^n steps] mJy/bm at 15.4 GHz, beam: 2.04×3.77 (mas) at $-26.53°$

Figure 7. Spectral index map of the year 2007 (right) and 2008 (left). The top panels show the spectral index fitted from all observing frequencies, and the bottom panels show the error in the fitting.

time coverage and frequency sampling around 15 GHz to test this hypothesis, but we observed a possible increase in RM with higher frequency. The extrapolated RM of the year 2006 to 43–22 GHz showed the same negative sign and rather similar magnitude as the previous 2 yr. In 2006, the component C10 moved into an optically thin region and contributed to the majority of observed Faraday rotation. This can be seen from the λ^2 dependence. Then, going into the year 2007, the C10 flux density decays to around half of C0, hence the core observed RM follows the emission of C0. This is further supported by the 15 GHz RM sign change to positive in 2007, with the decay of C10. The year 2007 also showed a broken RM fitting between 15 and 4 GHz, hence possibly probing at different regions/components at the unresolved core.

4.5 Jet fractional polarization

We observed that, in all epochs, the fractional polarization profile shows some degree of transverse gradient. The fractional polarization increases towards at least one of the jet edges, as in Fig. 1. This could be caused by several different scenarios, such as a shear/compression during jet–medium interaction, or the presence of a helical magnetic field. In addition, the fractional polarization gradient appears at the apparent jet bending position, at about 3.5 mas from the core.

Algaba et al. (2019) found that the jet trajectory follows a sinusoidal pattern, with a precession model providing a better fit. However, they do not have sufficient data to rule out helical structure, instabilities, or jet–medium interaction. Jet compression by ambient medium can increase synchrotron self-absorption, which can also lead to an inverted or flat spectrum (Mimica et al. 2009; Hovatta et al. 2014). Other indications of jet–medium interaction are the inverted spectrum of free–free absorption (Kino et al. 2021; Park et al. 2024), and spectral index gradient (O'Sullivan & Gabuzda 2009). For this purpose, we obtained the spectral index map of 2006,[2] 2007, and 2008. For 2007 and 2008, we used the same-beam registered Stokes I maps of all frequencies, and fitted the relation $S \propto \nu^\alpha$ to find the spectral index α. The error was determined through the conventional covariance matrix of the fit. The spectral index maps and their respective error are shown in Fig. 7. For 3 yr, we did not observe any spectral index gradient at the jet region, nor an inverted spectrum at the
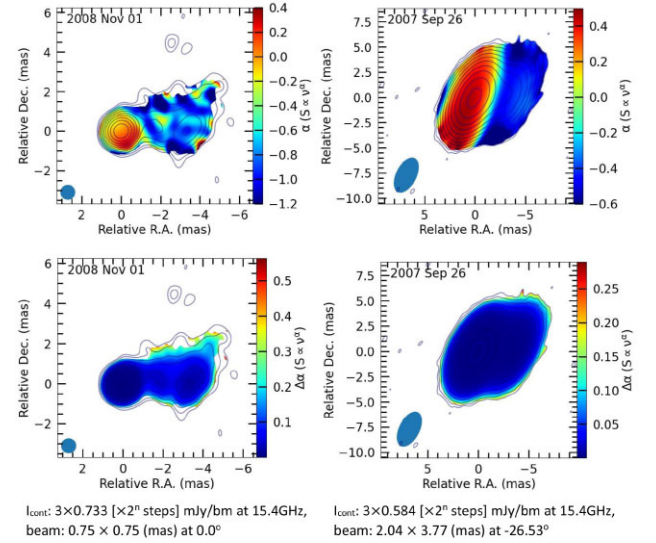
western edges of jets. Hence, we considered jet–medium interaction to be less likely, although we cannot rule out the possibility.

In Fig. 3, we observe depolarization at the jet's southern edge. The depolarization is only significant at 15 and 12 GHz. Beam depolarization by RM gradient cannot explain this, as a similar level of depolarization is not observed at the northern part of the slice. Hence, the apparent RM gradient cannot be confirmed through beam depolarization. In addition, the RM gradient is smaller than three beamwidths, hence not fully resolved (Zavala & Taylor 2003).

4.6 Origin of jet Faraday screen

For the jet region, we postulate an external Faraday screen. Here, we examine the possibility of a foreground cloud using variability arguments. The RM change in the jet region does not correlate with the RM change in the core region. Hence, we considered that if the Faraday rotation is to be caused by the foreground cloud, the size would be around ∼2 mas, or a maximum ∼17 pc. Hence, using a toy model we estimate the fluctuation in physical parameters to reproduce the observed RM change. The major RM changes happened between 2006 and 2007, with a change in magnitude |RM| of about 380 rad m^{-2}, with a sign change from positive to negative. The magnetic field strength obtained by Algaba et al. (2018) through synchrotron self-absorption analysis is $B_{SSA} = 0.07$ mG. We will use this value as the upper limit for magnetic field strength, as the strength is expected to decrease downstream toward the jet region that we observe. For electron density, the fiducial estimate we used is the value at Bondi radius, in M87[3] (Russell et al. 2015). We then extrapolated to the jet region using the scaling relation of electron density with distance along the jet. The Bondi radius can be obtained using $r_B = 2GM/c_s^2$, where the sound speed is $c_s = \sqrt{\gamma k_B T / \mu m_p}$ (Bondi 1952), M is the black hole mass $M = 1.0 \times 10^9 \, M_\odot$ (Zamaninasab et al. 2014), $\gamma = 5/3$ is the adiabatic index of the accreting gas, $\mu = 0.6$ is the mean molecular weight, m_p is the proton mass, and $T = 3.5 \times 10^6$ K (Bednarek &

---

[2]https://www.cv.nrao.edu/MOJAVE/spmaps/1633 + 382.2006_09_06_alpha_paper_gray.png

[3]We note that the initial approximation of n_e is based on a Fanaroff–Riley I (FRI) object, while our 1633+382 is an FRII, which often showed signatures of mergers (Baldi & Capetti 2008; Ramos Almeida et al. 2012).

Kirk [1995]). The estimated $r_B \sim 110$ pc or 0.6 mas projected, where the core region lies within the Bondi radius. Then we assumed the electron density n_e at Bondi radius is 0.5 cm^{-3} (Russell et al. [2015]), the scaling of $n_e \propto d^{-n}$, where $n = 2$. Hence, at the jet region, the electron density would be around 0.014 cm^{-3}.

Then we estimated the fluctuation in electron density/magnetic field needed to reproduce the |RM| change of 380 rad m^{-2}. First, we assumed that both the path-length $l = 0.1$ kpc and the magnetic field $B = 0.07$ mG are constant, with only the electron density is changing (from the initial value of $n_e = 0.014$ cm^{-3} as obtained). Then we would need a change in electron density of $\Delta n_e = 0.066$ cm^{-3} to reproduce the observed |RM| change from year 2006 to 2007. The change would be significantly larger than the n_e expected in the region. If, in turn, we assume the path-length and electron density to be constant, then the magnetic field strength must fluctuate by ~ 0.33 mG (from the initial of 0.07 mG).

Another approach to estimate the electron density and magnetic field fluctuation is to assume the equipartition condition. Here we assumed that the total internal energy is equal to the magnetic field energy density, $n_e \sim B^2$. With this condition, the change in electron density is dependent on magnetic field strength, or vice versa. Using Δ|RM| $= 387$ rad m^{-2}, $n_e = 0.014$ cm^{-3}, and $B = 0.07$ mG, we obtained the $\Delta B = 0.2$ mG and $\Delta n_e = 0.028$ cm^{-3}.

For both of the above estimates of the electron density and magnetic field, the fluctuation will be much larger if the path-length l is the size of ~ 17 pc, or of the same order of magnitude. Given the uncertainties of different estimates, long-term component monitoring would be crucial to definitely rule out a foreground cloud as a Faraday screen.

Another alternative explanation for |RM| and sign variability is the change in viewing angle, either intrinsically or caused by acceleration (O'Sullivan & Gabuzda [2009]). Regarding the source kinematics, models such as linear, helical, or precessing trajectories have been explored (Liu et al. [2010]; Algaba et al. [2019]). The change in viewing angle is naturally expected if the jet is following a helical trajectory. A jet encountering ambient medium and being deflected will also change its propagating angle. The observed jet region is located right at the apparent bending position, where the jet downstream turns north-west direction. Here, we cannot explore the kinematics of the jet region in more detail, which is only partially resolved with the current resolution. Broderick & Loeb ([2009]) explored another alternative, which is the relativistic helical bulk motion of the Faraday rotating jet sheath. They showed that the |RM| and sign can change with viewing angle concerning the Faraday rotating medium, with an asymmetric transverse RM profile. Here, we do not have sufficient resolution to obtain a reliable transverse RM profile. The jet RM in the years 2006, 2007, and 2008 does not show significant spatial structure; this could be intrinsic, or the low-resolution smoothing out the structure. Better resolution and sensitivity will greatly help us to uncover these possibilities.

5 CONCLUSIONS

In this investigation, we focus on the RM variability from 2004 to 2008. For this purpose, we used multifrequency polarization observation from 4 to 43 GHz with the VLBA. We consistently detected RM in the core region for 5 yr. For the jet region, we only detected RM located at the jet feature about 3.5 mas from the core during 2006, 2007, and 2008. We also observe that the RM changes in both magnitude and sign, with no apparent transverse structure, except in the jet region of 2008.

At the core region, the 43–22 GHz RM magnitude is consistent within at least 3 yr of observation, but from 2007 onward, the RM sign changes from negative to positive. For RM around 15 GHz, the emerging component C10 contributed briefly to the linear λ^2 law in the year 2006. The C10 flux density then decayed to below the core flux density in 2007 onward, hence deviation from the linear λ^2 law, and a sign change are observed. The 2007 power index a (for a in RM $\propto \nu^a$) was found to be around 1.48 ± 1.40, which is consistent with $a \sim 2$, suggesting the equipartition condition in the jet sheath. For the jet region, high fractional polarization and linear λ^2 law of EVPA were observed, hence the situation of an external Faraday screen is more likely. Jet–medium interaction and foreground cloud are less likely to be the Faraday screen, based on the large fluctuation n_e and magnetic field needed to reproduce the observed RM changes. Alternative explanations based on jet kinematics are discussed. Higher resolution and better cadence are needed for a more complete investigation of this aspect.

DATA AVAILABILITY

The data underlying this article are available in the NRAO Data Archive, at https://data.nrao.edu/portal/, under project codes BG152, BK107f, BL123B, BL137i, BG173b, and BA089. The VLBA 15 GHz data collected at the MOJAVE program are available at https://www.cv.nrao.edu/MOJAVE/. The VLBA 43 GHz data collected by the VLBA-BU-BLAZAR monitoring program are available at https://www.bu.edu/blazars/BEAM-ME.html.

REFERENCES

Algaba J. C., 2013, MNRAS, 429, 3551
Algaba J. C., Gabuzda D. C., Smith P. S., 2012, MNRAS, 420, 542
Algaba J.-C. et al., 2018, ApJ, 859, 128
Algaba J. C., Rani B., Lee S. S., Kino M., Park J., Kim J.-Y., 2019, ApJ, 886, 85
Aller M. F., Aller H. D., Hughes P. A., 1992, ApJ, 399, 16
Asada K., Inoue M., Kameno S., Nagai H., 2008a, ApJ, 675, 79
Asada K., Inoue M., Nakamura M., Kameno S., Nagai H., 2008b, ApJ, 682, 798
Baldi R. D., Capetti A., 2008, A&A, 489, 989
Bednarek W., Kirk J. G., 1995, A&A, 294, 366
Bondi H., 1952, MNRAS, 112, 195
Broderick A. E., Loeb A., 2009, ApJ, 703, L104
Charlot P., Gabuzda D. C., Sol H., Degrange B., Piron F., 2006, A&A, 457, 455
Chen Y., Zhang X., Zhang H., Xiong D., Yu X., Cha Y., Li B., Huang X., 2015, Ap&SS, 357, 100
Coughlan C. P., Gabuzda D. C., 2013, EPJ Web Conf., 61, 07009
Croke S. M., Gabuzda D. C., 2008, MNRAS, 386, 619
Fan J. H., Liu Y., Yang J. H., Yuan Y. H., Li Y., Zhang Q. F., 2013, in Zhang C., Belloni T., Méndez M., Zhang S., eds, Proc. IAU Symp. Vol. 290,

Feeding Compact Objects: Accretion on All Scales. Cambridge Univ. Press, Cambridge, p. 209

Fomalont E. B., 1999, in Taylor G. B., Carilli C. L., Perley R. A., eds, ASP Conf. Ser. Vol. 180, Synthesis Imaging in Radio Astronomy II. Astron. Soc. Pac., San Francisco, p. 301

Foschini L., 2011, Res. Astron. Astrophys., 11, 1266

Gabuzda D. C., Gómez J. L., 2001, MNRAS, 320, L49

Gabuzda D. C., Kochanev P. Y., 1997, Vistas Astron., 41, 219

Gabuzda D. C., Kochenov P. Y., Cawthorne T. V., Kollgaard R. I., 2000a, MNRAS, 313, 627

Gabuzda D. C., Kochenov P. Y., Kollgaard R. I., Cawthorne T. V., 2000b, MNRAS, 315, 229

Gabuzda D. C., Kochenov P. Y., Cawthorne T. V., 2000c, MNRAS, 319, 1125

Gómez J.-L., Marscher A. P., Alberdi S. G., Jorstad S. G., Agudo I., 1992, NRAO VLBA Sci. Memo., #30, 1

Gómez J. L., Marscher A. P., Jorstad S. G., Agudo I., Roca-Sogorb M., 2008, ApJ, 681, L69

Gómez J. L., Roca-Sogorb M., Agudo I., Marscher A. P., Jorstad S. G., 2011, ApJ, 733, 11

Hewett P. C., Wild V., 2010, MNRAS, 405, 2302

Homan D. C., Ojha R., Wardle J. F. C., Roberts D. H., Aller M. F., Aller H. D., Hughes P. A., 2002, ApJ, 568, 99

Hovatta T., Valtaoja E., Tornikoski M., Lähteenmäki A., 2009, A&A, 494, 527

Hovatta T., Lister M. L., Aller M. F., Aller H. D., Homan D. C., Kovalev Y. Y., Pushkarev A. B., Savolainen T., 2012, AJ, 144, 105

Hovatta T. et al., 2014, AJ, 147, 143

Jorstad S. G. et al., 2007, AJ, 134, 799

Kim J.-Y., 2014, J. Korean Astron. Soc., 47, 195

Kino M. et al., 2021, ApJ, 920, L24

Kovalev Y. Y. et al., 2005, AJ, 130, 2473

Lee S.-S., Lobanov A. P., Krichbaum T. P., Witzel A., Zensus A., Bremer M., Greve A., Grewing M., 2008, AJ, 136, 159

Leppanen K. J., Zensus J. A., Diamond P. J., 1995, AJ, 110, 2479

Lico R. et al., 2014, A&A, 571, A54

Lisakov M. M., Kravchenko E. V., Pushkarev A. B., Kovalev Y. Y., Savolainen T. K., Lister M. L., 2021, ApJ, 910, 35

Lister M. L. et al., 2009, AJ, 138, 1874

Lister M. L., Aller M. F., Aller H. D., Hodge M. A., Homan D. C., Kovalev Y. Y., Pushkarev A. B., Savolainen T., 2018, ApJS, 234, 12

Lister M. L., Homan D. C., Kellermann K. I., Kovalev Y. Y., Pushkarev A. B., Ros E., Savolainen T., 2021, ApJ, 923, 30

Liu Y., Jiang D. R., Shen Z.-Q., Karouzos M., 2010, A&A, 522, A5

Lobanov A. P., 1998, A&A, 330, 79

Mahmud M., Coughlan C. P., Murphy E., Gabuzda D. C., Hallahan D. R., 2013, MNRAS, 431, 695

Martí-Vidal I., Pérez-Torres M. A., Lobanov A. P., 2012, A&A, 541, A135

Mimica P., Aloy M. A., Agudo I., Marti J. M., Gómez J. L., Miralles J. A., 2009, ApJ, 696, 1142

O'Sullivan S. P., Gabuzda D. C., 2009, MNRAS, 393, 429

Park J., Hada K., Kino M., Nakamura M., Ro H., Trippe S., 2019, ApJ, 871, 257

Park J., Kino M., Nagai H., Nakamura M., Asada K., Kam M., Hodgson J. A., 2024, A&A, 685, A115

Pratley L., Johnston-Hollitt M., 2016, MNRAS, 462, 3483

Ramos Almeida C. et al., 2012, MNRAS, 419, 687

Russell H. R., Fabian A. C., McNamara B. R., Broderick A. E., 2015, MNRAS, 451, 588

Volvach A. E., Bychkova V. S., Kardashev N. S., Larionov M. G., Vlasyuk V. V., Spiridonova O. I., 2009, Astron. Rep., 53, 401

Walker R. C., Dhawan V., Romney J. D., Kellermann K. I., Vermeulen R. C., 2000, ApJ, 530, 233

Wardle J. F. C., Kronberg P. P., 1974, ApJ, 194, 249

Zamaninasab M., Clausen-Brown E., Savolainen T., Tchekhovskoy A., 2014, Nature, 510, 126

Zavala R. T., Taylor G. B., 2003, ApJ, 589, 126

Zavala R. T., Taylor G. B., 2004, ApJ, 612, 749

APPENDIX A: DATA CALIBRATION OF YEAR 2005

For the 2005 data, we combined two separate observations spaced apart by 3 d. The question may arise from the intraday variability of total intensity observed by Volvach et al. (2009). In the literature, rapid variability of cm-wave very long baseline interferometry polarization was largely observed for BL Lac object, from intraday variability (Gabuzda & Kochanev 1997; Gabuzda et al. 2000a,b; Gabuzda, Kochenov & Cawthorne 2000c) to weeks (Charlot et al. 2006). However, no literature was found for polarization angle variability for 1633+382. Long-term monitoring by the MOJAVE project (Lister et al. 2018) had shown that throughout the year 2005, the 15 GHz EVPA had been consistent between 40° and 47°. Hence,
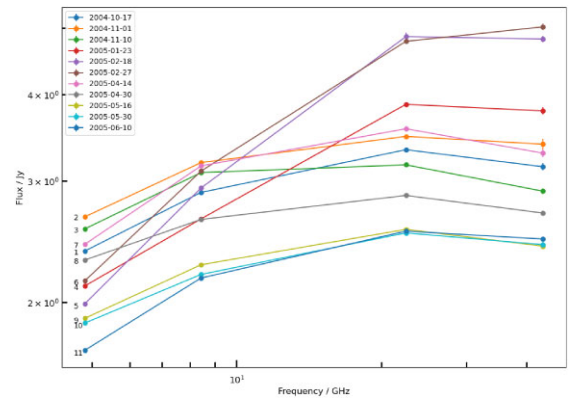

Figure A1. VLA integrated total intensity of 1749+096, for frequencies 4.8, 804, 22.4, and 43.3 GHz. The label number 1 corresponds to date 2004 October 17, and the subsequent labels follow the order of observation date. The spectral index rise started from 2005 January 23, reaching the largest spectral index $\alpha \sim 0.4$ at the end of 2005 February, then flattened in 2005 April.
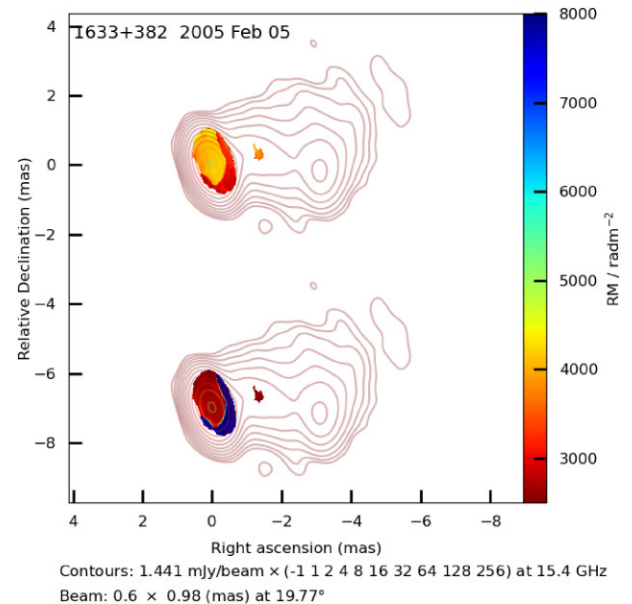

Figure A2. RM fitted without 90° rotation. The upper plot is the RM map, and the lower plot is the RM error. The core RM is roughly separated into region of 4500 and 3000 rad m^{-2}, and the error at 2500 and 8000 rad m^{-2}.

we try to approximate the stability to 22 and 43 GHz in the year 2005.

The 15 GHz data and CLEAN model were obtained from the MOJAVE website, under the project name BL123B. For 22 and 43 GHz, the calibration was done as in the standard AIPS calibration package for polarization, and EVPA correction using data from the VLA POLCAL project. For 22 and 43 GHz, a 90° rotation was added to the final EVPA correction, due to the optically thin/thick transition (Gabuzda & Gómez 2001). This is based on the suggested opacity change in EVPA calibrator 1749+096, as shown in Fig. A1. We assumed that the transition only affects the higher frequencies, 22

and 43 GHz. This is further supported by the EVPA stability of 15 GHz throughout the year 2005 as mentioned in the previous paragraph. Then for 1633+382, the RM fitted without 90° rotation also shows gross discontinuity and large error, as in Fig. A2.

APPENDIX B: COMPLEX CLEANING

The method of complex CLEANING was developed by Pratley & Johnston-Hollitt (2016). Complex CLEAN is superior than the standard polarization CLEAN method in that it is rotationally invariant, detects more components at low signal-to-noise ratio, and also has
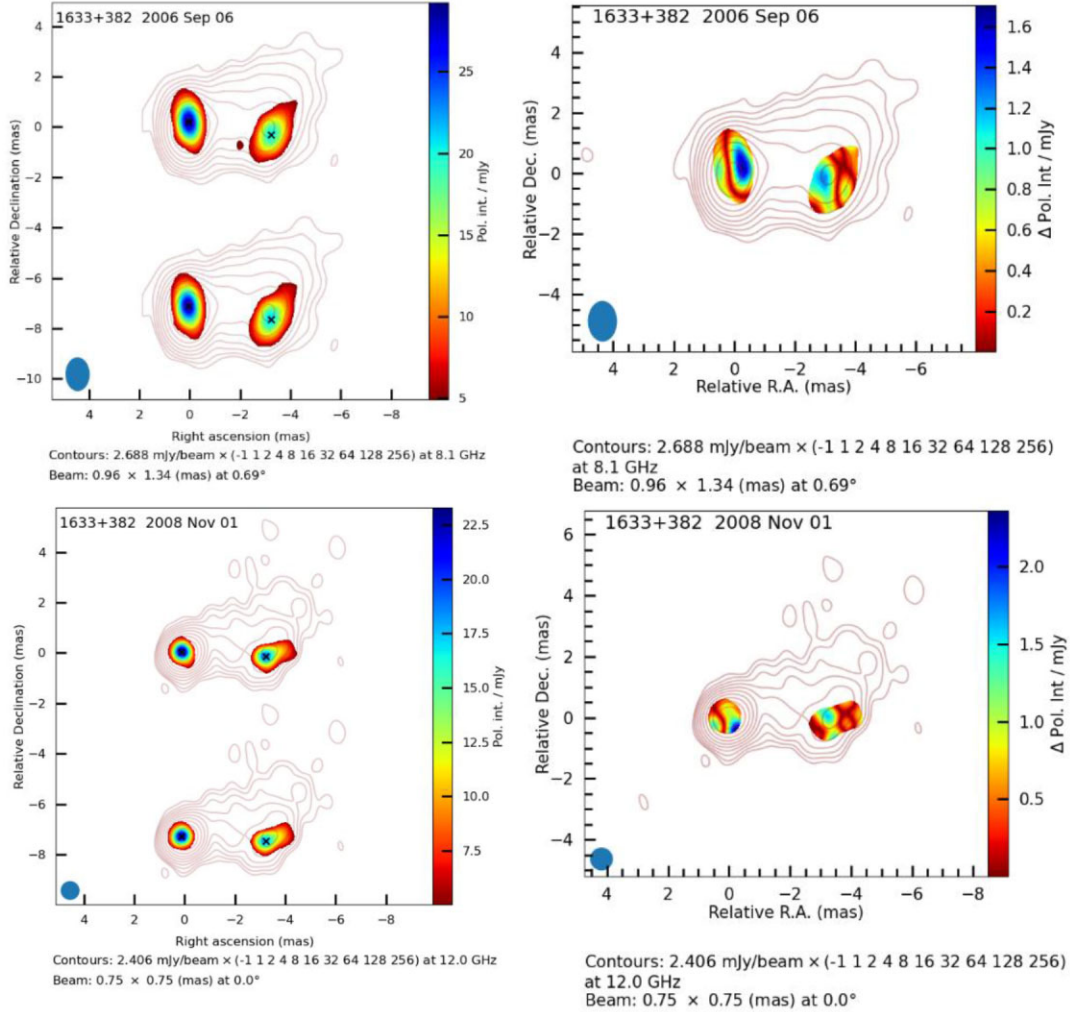

Figure B1. Left column: BL137I 8.1 GHz (top) and BA089 12.0 GHz (bottom) were shown. In a single frame, the colour scale image above is the polarized intensity image for the complex CLEAN method, at below is the standard polarization CLEAN method. The same total intensity contour was plotted for both colour images to facilitate comparison. The black cross at the centre of the core and jet indicates the position where the test values were taken. The beam size was represented as a circle at the bottom left corner. Right column: The absolute value of the difference between complex CLEAN and standard polarization CLEAN is shown in a colour scale.

Table B1. Result from standard polarization CLEANING and complex CLEANING.

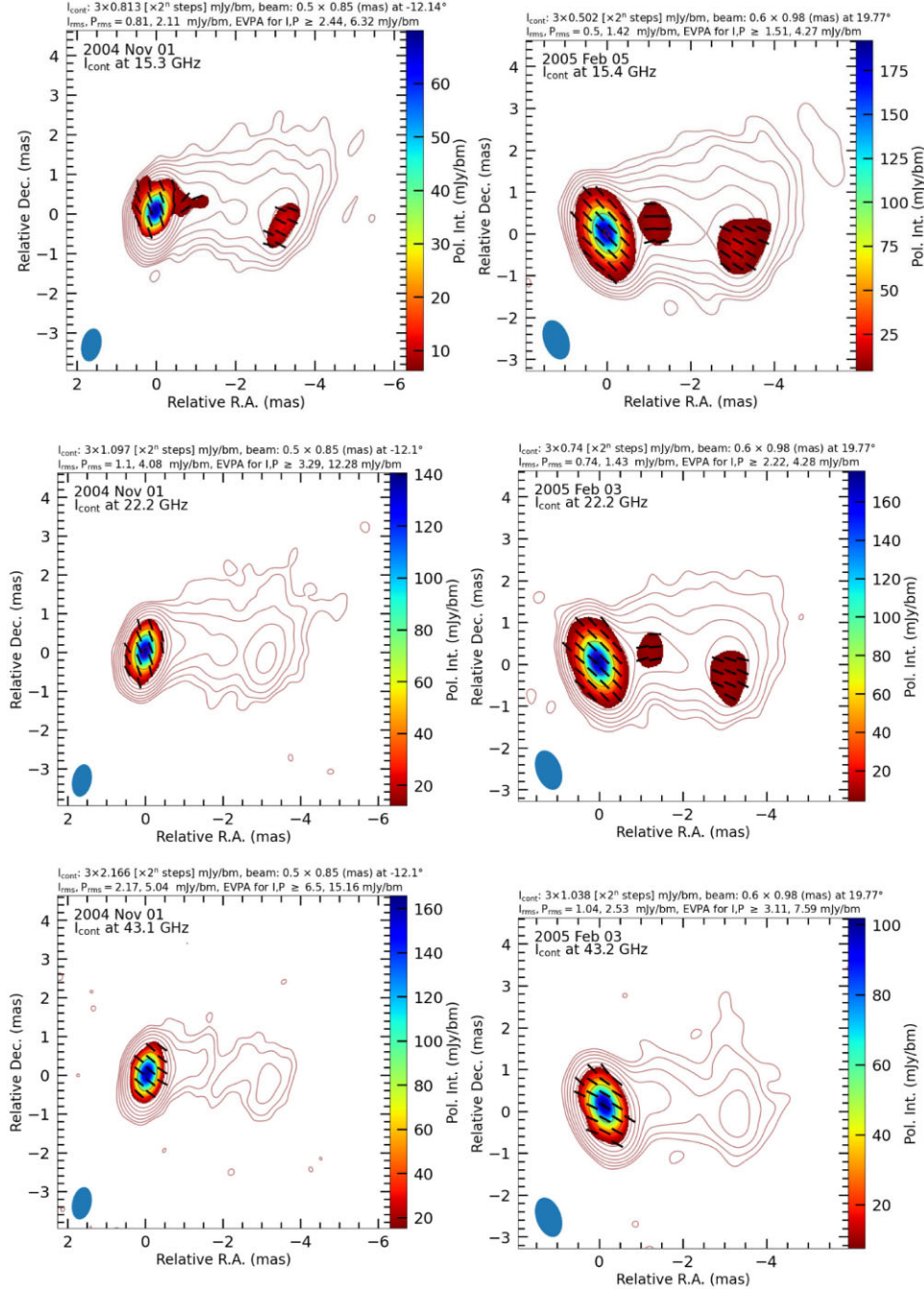| Project	CLEAN	$\chi_{integrated}$ (°)				$\chi_{test,core}$ (°)				$\chi_{test,jet}$ (°)		
		χ_{12}	χ_{15}	χ_{22}	χ_{24}	χ_{12}	χ_{15}	χ_{22}	χ_{24}			
BL137I	Standard	39 ± 3	41 ± 3	58 ± 6	75 ± 7	31 ± 1	34 ± 2	52 ± 2	68 ± 2	51 ± 2	52 ± 2	67 ± 2	78 ± 2
	Complex	43 ± 3	44 ± 3	62 ± 6	76 ± 7	32 ± 2	34 ± 2	53 ± 2	68 ± 2	53 ± 2	52 ± 2	67 ± 2	75 ± 3
BA089	Standard	61 ± 4	52 ± 5	57 ± 8	49 ± 4	65 ± 3	61 ± 3	–	54 ± 5	63 ± 2	63 ± 2	62 ± 4	60 ± 3
	Complex	65 ± 4	54 ± 5	74 ± 8	61 ± 4	67 ± 3	61 ± 3	–	68 ± 5	66 ± 2	63 ± 2	61 ± 4	63 ± 3

Figure C1. Tick mark of uniform length representing the observed EVPA, overlaid on polarized intensity colour map, at the indicated frequency. The polarized intensity was blanked on a 3σ level. The contours show the Stokes I at $3\sigma \times 2^n$ steps.

fewer spurious components. We used the final calibrated data of 1633+382 from project BA089 and BL137I, convolved with their respective beam as in Table 1 as our test data. The complex CLEANING was carried out in MIRIAD. Then, both set of data were run through the same Rician debiasing process and blanked. We compared the integrated EVPA, EVPA test point at core, and jet. The test point was chosen through eyeballing the polarization intensity peak in the core and jet. Noted that the test value was taken from the same position, both in standard and complex CLEAN methods. As shown in Fig. B1 and Table B1, the EVPA difference between the two CLEANINGs is within the error. Although the difference in integrated EVPA is larger, only in

two instances of project BA089 the difference is larger than $10°$. We attributed the small differences to high SNR and the compact nature of our source component. Hence, we concluded the standard polarization CLEAN method would not introduce significant error in this study.
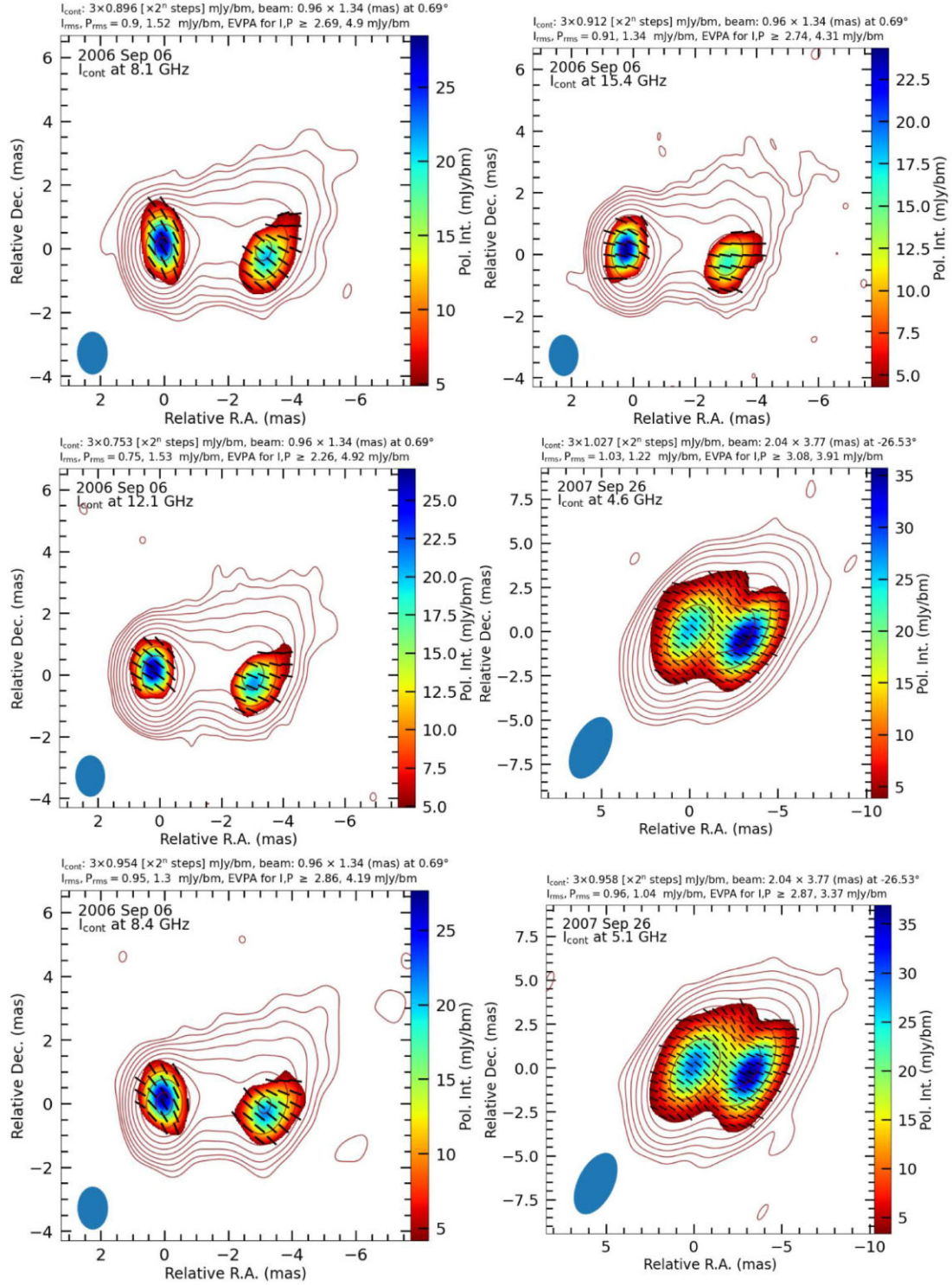
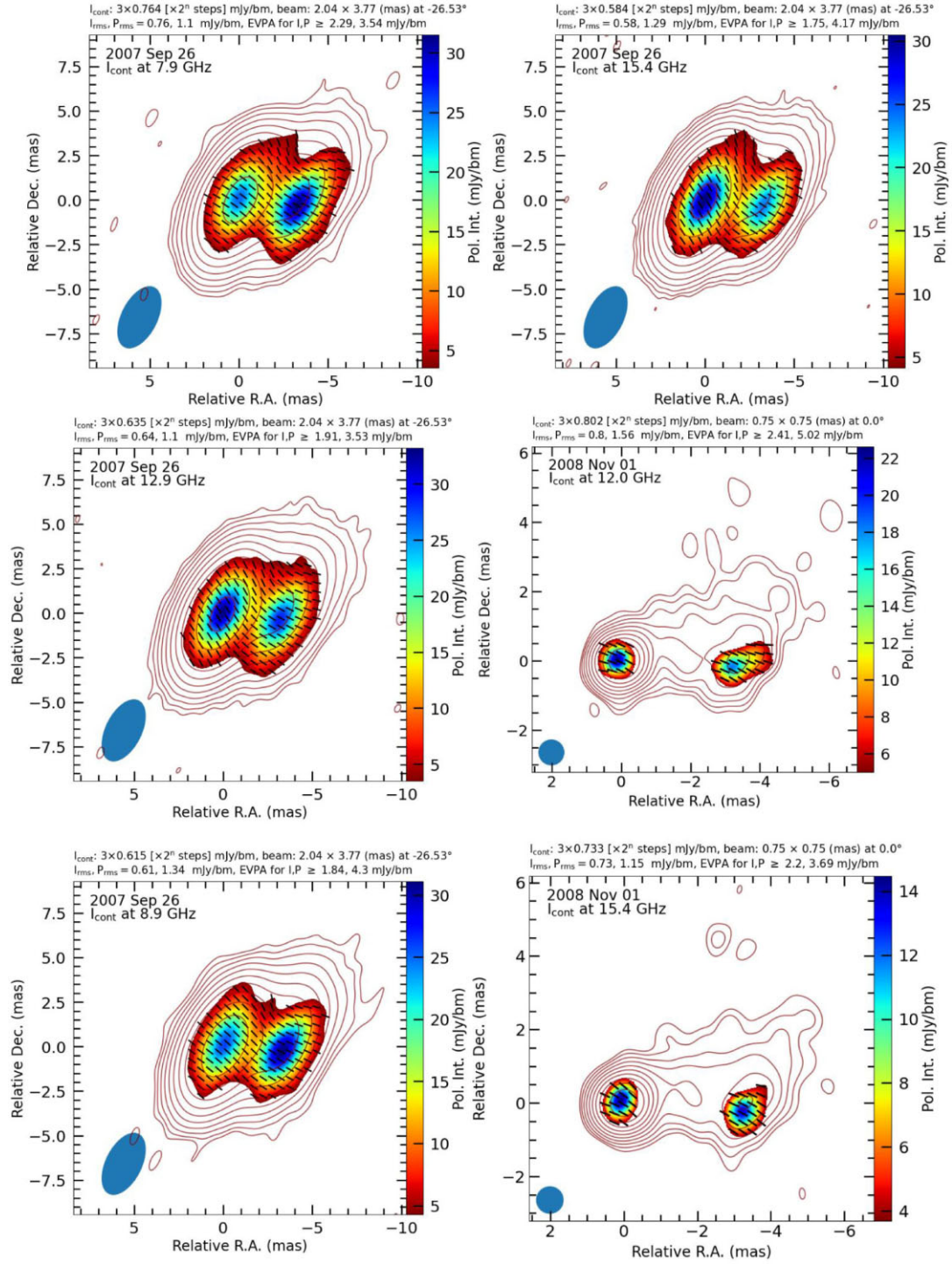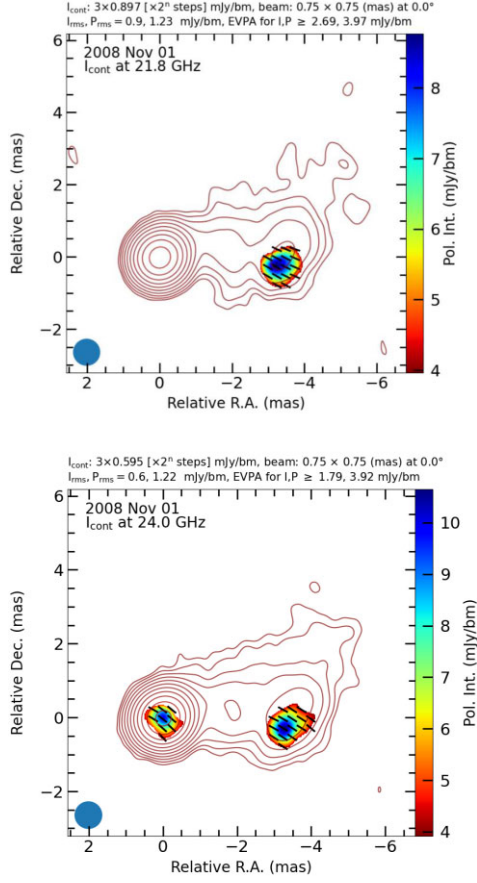## APPENDIX C: EVPA AND POLARIZED INTENSITY MAPS

Figure C1. (*continued*).

Figure C1. (*continued*).

I_cont: 3×0.897 [×2^n steps] mJy/bm, beam: 0.75 × 0.75 (mas) at 0.0°
I_rms, P_rms = 0.9, 1.23 mJy/bm, EVPA for I,P ≥ 2.69, 3.97 mJy/bm

2008 Nov 01
I_cont at 21.8 GHz

I_cont: 3×0.595 [×2^n steps] mJy/bm, beam: 0.75 × 0.75 (mas) at 0.0°
I_rms, P_rms = 0.6, 1.22 mJy/bm, EVPA for I,P ≥ 1.79, 3.92 mJy/bm

2008 Nov 01
I_cont at 24.0 GHz

Figure C1. (*continued*).
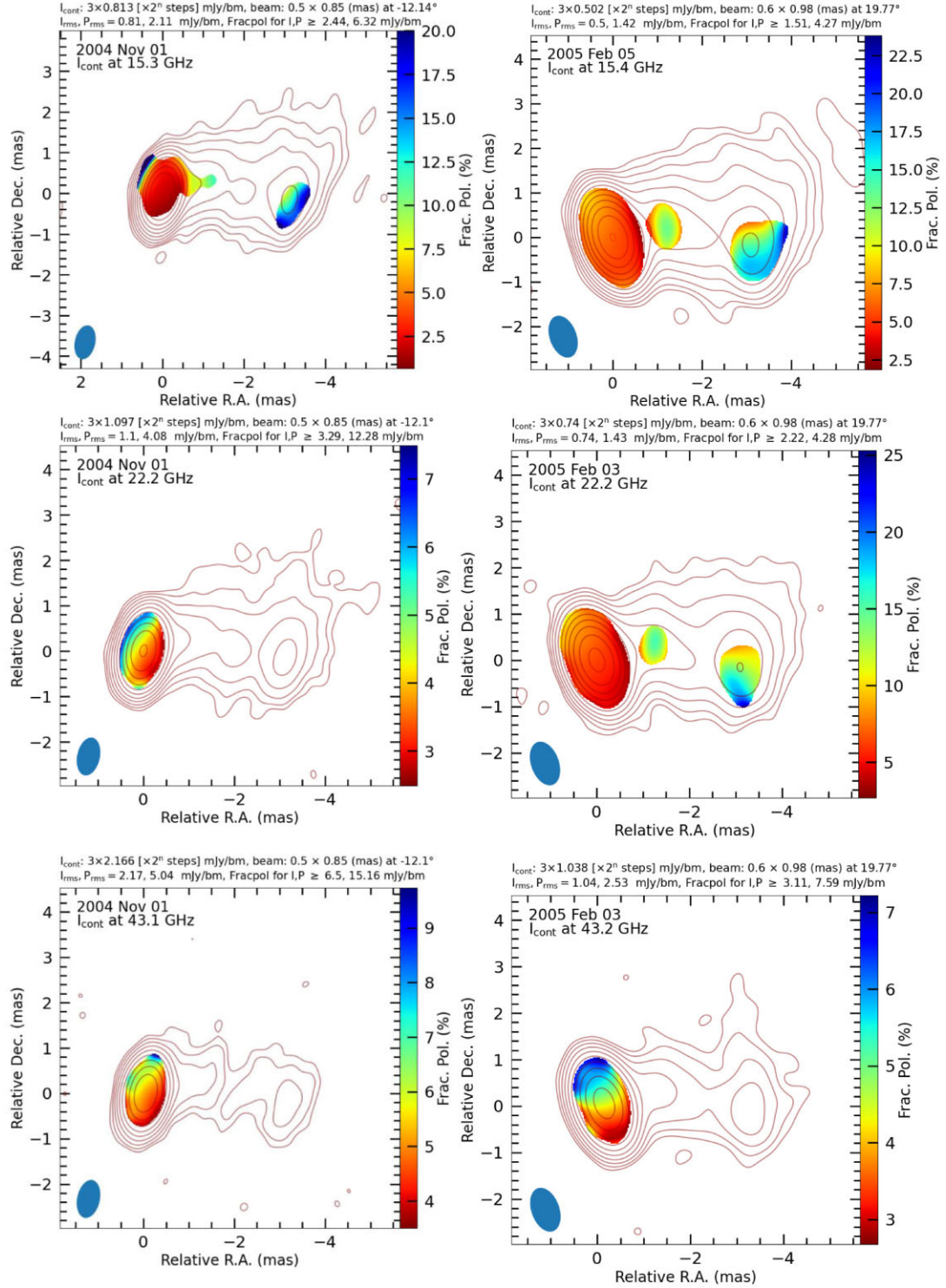
Figure D1. Fractional polarization maps, and the contours represent Stokes *I*. Note that in some maps the fractional polarization gradient at the core region is not seen because of its low value compared to the jet region.
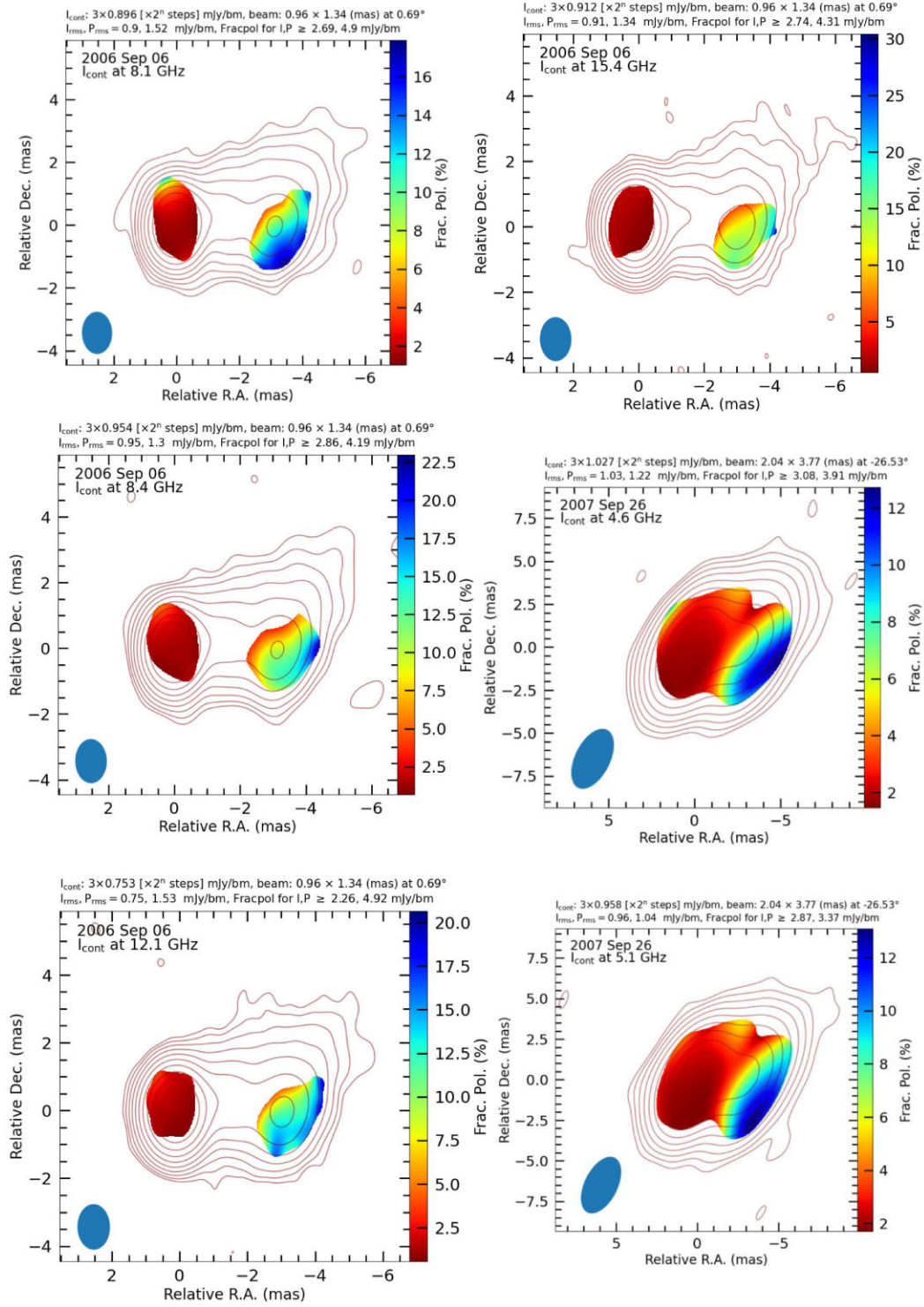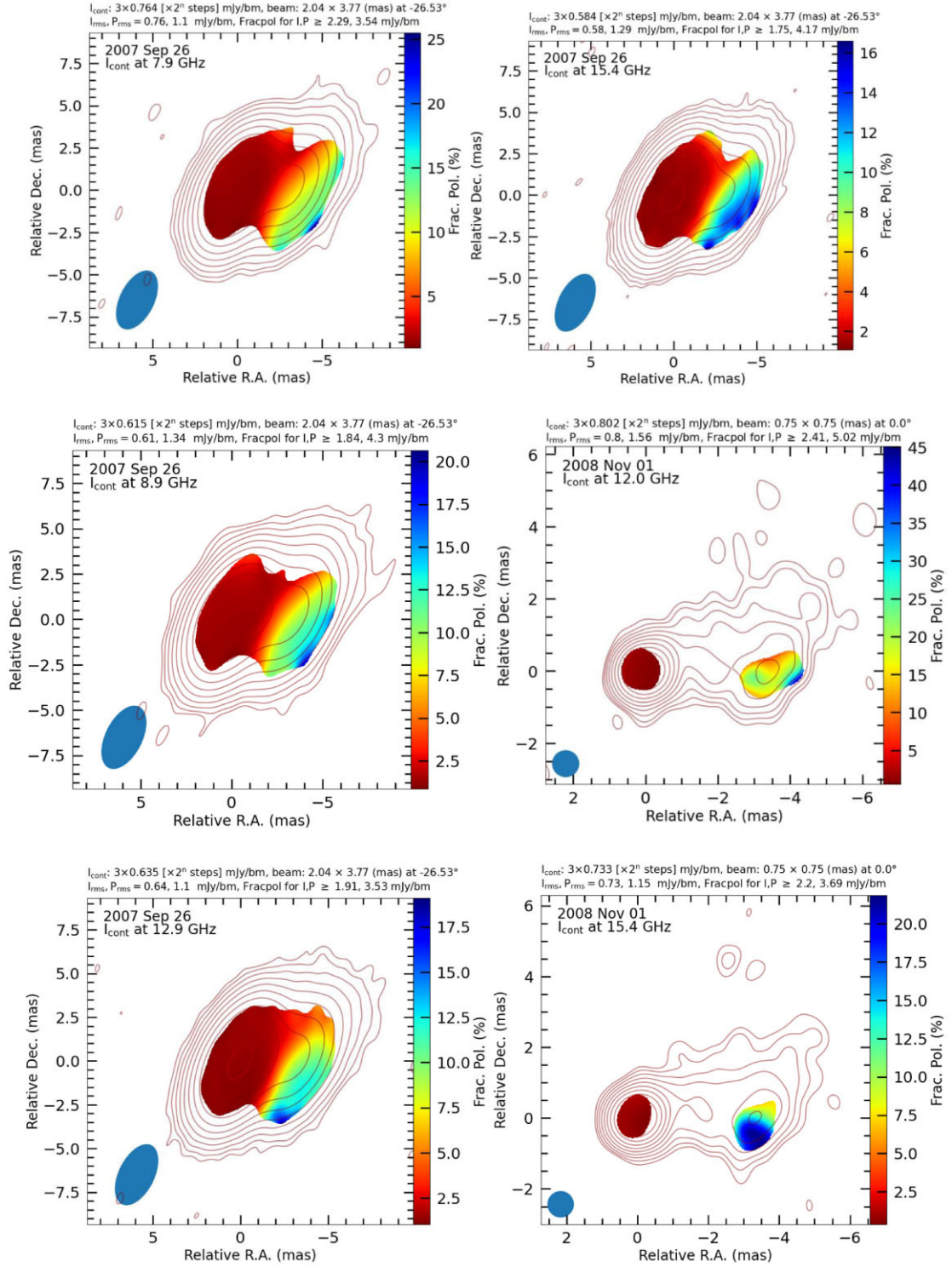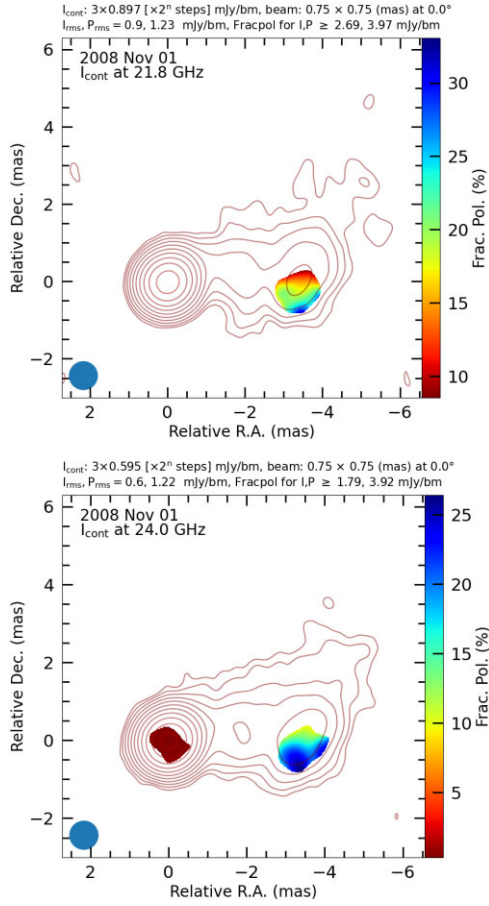
Figure D1. (*continued*).

Figure D1. (*continued*).

Figure D1. (*continued*).

This paper has been typeset from a TEX/LATEX file prepared by the author.